What drives the redshift evolution of strong emission line ratios?

Fuyan Bian,[1,2]★ Lisa J. Kewley,[2,3] Brent Groves[2,3] and Michael A. Dopita [2,3]†

[1]*European Southern Observatory, Alonso de Córdova 3107, Casilla 19001, Vitacura, Santiago 19, Chile*
[2]*Research School of Astronomy & Astrophysics, Mt Stromlo Observatory, Australian National University, Canberra, ACT 2611, Australia*
[3]*ARC Centre of Excellence for All Sky Astrophysics in 3 Dimensions (ASTRO 3D), Canberra, ACT 2611, Australia*

ABSTRACT

We study the physical mechanisms that cause the offset between low-redshift and high-redshift galaxies on the [O III] λ5007/Hβ versus [N II] λ6584/Hα 'Baldwin, Phillips & Terlevich' (BPT) diagram using a sample of local analogues of high-redshift galaxies. These high-redshift analogue galaxies are selected from the Sloan Digital Sky Survey. Located in the same region on the BPT diagram as the ultraviolet selected galaxies at $z \sim 2$, these high-redshift analogue galaxies provide an ideal local benchmark to study the offset between the local and high-redshift galaxies on the BPT diagram. We compare the nitrogen-to-oxygen ratio (N/O), the shape of the ionizing radiation field, and ionization parameters between the high-redshift analogues and a sample of local reference galaxies. The higher ionization parameter in the high-redshift analogues is the dominant physical mechanism driving the BPT offset from low- to high-redshift, particularly at high [N II] λ6584/Hα. Furthermore, the N/O ratio enhancement also plays a minor role to cause the BPT offset. However, the shape of the ionizing radiation field is unlikely to cause the BPT offset because the high-redshift analogues have a similar hard ionizing radiation field as local reference galaxies. This hard radiation field cannot be produced by the current standard stellar synthesis models. The stellar rotation and binarity may help solve the discrepancy.

Key words: ISM: abundances – ISM: evolution – galaxies: abundances – galaxies: high-redshift – galaxies: ISM.

1 INTRODUCTION

Optical recombination and collisionally excited emission lines provide essential information to study the properties of the ionized interstellar medium (ISM) and ionizing radiation field. The relative strength of these emission lines is regulated by the shape of the ionizing radiation field, gas-phase chemical abundance, gas density, and ionization parameter (the ratio of the ionizing photon number density to the hydrogen number density).

The 'Baldwin, Phillips & Terlevich' (BPT; Baldwin, Phillips & Terlevich 1981) diagrams are powerful tools to separate star-forming galaxies and active galactic nuclei (AGNs; e.g. Veilleux & Osterbrock 1987). Galaxies at $z \sim 0$ are located in a well-defined star-forming sequence at on the [O III] λ5007/Hβ versus [N II] λ6584/Hα BPT diagram (e.g. Kewley et al. 2006; Stasińska et al. 2006). However, galaxies at $z \sim 2$ do not share the same location of their local counterparts on the BPT diagram (e.g. Erb et al. 2006; Liu et al. 2008; Hainline et al. 2009; Bian et al. 2010;

Steidel et al. 2014; Shapley et al. 2015). For a fixed [N II] λ6584/Hα ratio, high-redshift galaxies tend to have a higher [O III] λ5007/Hβ ratio, and vice versa. Understanding the dominant mechanism of cause this offset would provide valuable insight into how the stellar population, metal abundance, and star formation environment of galaxies evolve with cosmic time.

The physical mechanism driving this offset is still under debate. Four competing interpretations have been proposed: (1) higher nitrogen-to-oxygen ratio (N/O ratio; e.g. Masters et al. 2014; Jones, Martin & Cooper 2015; Shapley et al. 2015; Masters, Faisst & Capak 2016; Kojima et al. 2017), (2) harder stellar radiation field (e.g. Steidel et al. 2014, 2016), (3) higher ionization parameter and/or electron density in high-redshift galaxies (e.g. Brinchmann, Pettini & Charlot 2008; Liu et al. 2008; Bian et al. 2010; Kewley et al. 2013a, b; Dopita et al. 2016; Kojima et al. 2017), and (4) selection effects (e.g. Juneau et al. 2014; Salim et al. 2015).

Bian et al. (2016) found that selection effects cannot fully account for the offset between low- and high-redshift galaxies on the BPT diagram. Only less than 50 per cent of the galaxies selected from the Sloan Digital Sky Survey (SDSS) with the same emission line luminosities or ultraviolet (UV) luminosities as high-redshift
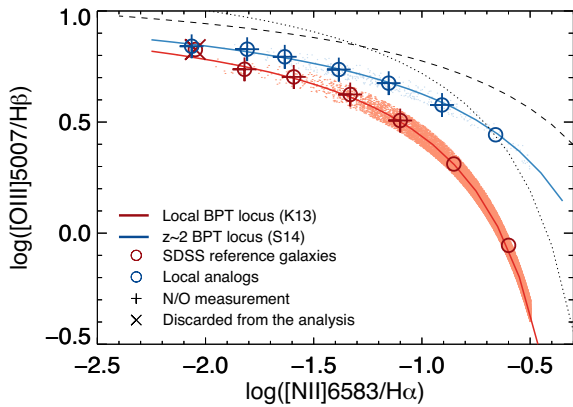
★ E-mail: fbian@eso.org
† Deceased

Figure 1. BPT diagnostic diagram of local analogues of high-redshift galaxies and the SDSS reference galaxies. The small blue and red points represent the individual local analogues and the SDSS reference galaxies, respectively. The blue and red open circles represent the stacked spectra of the local analogues and SDSS reference galaxies, respectively. The open circles with plus symbols are the stacked spectra with reliable N/O ratio and oxygen abundance measurements using the direct T_e method, and the open circle with 'x' symbol denotes the spectrum discarded from our analysis. The blue solid line represents the star-forming BPT locus at $z \sim 2$ adopted from Steidel et al. (2014), and the red solid line represents the local star-forming BPT locus adopted from Kewley et al. (2013a). The dotted and dashed lines represent the empirical (Kauffmann et al. 2003) and theoretical (Kewley et al. 2001) separations of star-forming galaxies and AGNs, respectively. A colour version of this figure is available online.

galaxies are located on the BPT star-forming sequence defined by $z \sim 2$ UV-selected galaxies (Steidel et al. 2014). Even if the selection effect can fully explain the offset, we still need to understand the physical mechanisms that cause it. Therefore, in this work, we focus on the first three of the interpretations of the observed BPT offset.

Strong optical emission lines, such as [O II] $\lambda3727$, [O III] $\lambda5007$, H β, H α, and [N II] $\lambda6584$, do not have the power to disentangle the above physical mechanisms, because these strong line ratios are highly degenerate with physical properties. For instance, a higher ionization parameter, or a harder radiation field, or an increased pressure in the H II region can increase the [O III] $\lambda5007$/H β ratio and shifts the low-redshift star-forming sequence to high-redshift star-forming sequence (e.g. Kewley et al. 2013a). Therefore, it is difficult to draw an exclusive conclusion based on these strong emission lines alone. In this work, we use a sample of local analogues of high-redshift galaxies to approach this issue. By stacking the spectra of these analogues and a sample of local reference galaxies, we are able to detect weak emission lines, including [O III] $\lambda4363$ and He II $\lambda4686$, which usually cannot be detected in high-redshift galaxies. These weak lines provide powerful probes in disentangling the different physical mechanisms causing the BPT offset between the low- and high-redshift galaxies.

2 METHOD

2.1 Sample selection

We select a sample of local analogues of high-redshift galaxies and low-redshift reference galaxies from the SDSS galaxy survey. These galaxies are selected based on their locations on the [O III]/H β versus [N II]/H α BPT diagram (Fig. 1). The local analogues are selected within the ±0.04 dex region of the $z \sim 2$ star-forming sequence defined by equation 9 in Steidel et al. (2014). The SDSS

reference galaxies are selected within the ±0.05 dex region of the $z \sim 0$ star-forming BPT sequence defined by equation 3 in Kewley et al. (2013b) (Fig. 1). We also use the [O III]/H β versus [S II]/H α and [O III]/H β versus [O I]/H α BPT diagnostic diagrams to remove potential contamination from shock/AGNs (Bian, Kewley & Dopita 2018). At last, a total of 443 galaxies are selected as local analogues of high-redshift galaxies, and a total of 22 428 galaxies are selected as local reference galaxies. These local analogues of high-redshift galaxies share similar trend with star-forming galaxies at $z \sim 2$ in all the diagnostic diagrams (e.g. Steidel et al. 2014, 2016; Shapley et al. 2015; Sanders et al. 2016a; Strom et al. 2017).

We summarize the physical properties of these high-redshift analogues as follows: the median stellar mass, star formation rate (SFR), and specific SFR (sSFR) of the sample of high-redshift analogous are $\log(M_*/M_\odot) = 8.8^{+0.06}_{-0.02}$, $3.9^{+0.7}_{-0.2}$ $M_\odot$ yr^{-1}, and $10.0^{+1.0}_{-0.5}$ Gyr^{-1}, respectively. Their sSFR is consistent with that in $z \sim 2$ star-forming galaxies with similar stellar mass (e.g. Rodighiero et al. 2011; Trainor et al. 2016), and these analogues follow the M_*–SFR relation at $z \sim 2.3$ (Sanders et al. 2020). It is worth noting that the local analogue selection is biased to the low stellar mass and low [N II] $\lambda6584$/H α ratio end comparing to the typical UV-selected or mass-selected galaxies at $z \sim 2$–3, as it is discussed in Strom et al. (2017). Actually, these analogues more closely resemble the properties of Ly α emitters and low-mass galaxies at $z \sim 2$–3 (e.g. Trainor et al. 2016). Particularly, the ionization parameters of these local analogues are in the range of $\log q = 7.7$–8.5 ($\log U = -2.7$ to $\log U = -2.0$), which are well in agreement with those in $z \sim 2.5$ Ly α emitters (e.g. Nakajima & Ouchi 2014; Trainor et al. 2016). Furthermore, Sanders et al. (2020) suggested that the metallicity calibrations derived from the direct T_e metallicity in these local analogues reliably reproduce the average properties of $z > 1$ galaxies with [O III] $\lambda4363$ auroral-line measurements, which are mostly low-mass galaxies.

Therefore, it is a reasonable assumption that the physical mechanisms driving the offset between the local analogues and local star-forming sequence are the same as those determining the observed location of high-redshift star-forming galaxies on the BPT diagram. This type of local analogues provides an excellent local laboratory and benchmark to understand the physical mechanism(s) to drive the evolution of the [O III]/H β versus [N II]/H α BPT diagram between low- and high-redshift galaxies.

2.2 Stacked spectra

By combining individual spectra we can detect the weak emission lines, including [O III] $\lambda4363$ and He II $\lambda4686$. The analogues of high-redshift galaxies and the SDSS reference galaxies have been divided into seven bins of 0.25 dex in the range -2.25 to -0.25 in their [N II]/H α ratios. We refer the readers to tables 3 and 4 in Bian et al. (2018) for detailed properties of galaxies in each of the [N II]/H α bins. We generate the stacked spectra in each [N II]/H α bin as follows. Each one-dimensional galaxy spectrum from the SDSS survey is deredshifted and dereddened based upon the Balmer decrement. The galaxy spectra are then normalized at the wavelength range between 4400 and 4450 Å. Finally, the spectra are combined by averaging the individual spectra in each [N II]/H α bin.

We measure the line fluxes in the stacked spectra. The stellar continuum of each stacked spectrum is fitted using the STARLIGHT stellar population synthesis code (Cid Fernandes et al. 2005) locally and then subtracted from the stacked spectra. Then the emission lines are fitted using Gaussian profiles to measure the line fluxes.

Only two galaxies in the sample of local reference galaxy fall into the $-2.00 < \log([\text{N\,\textsc{ii}}]/\text{H}\alpha) < -2.25$ bin, and both of them are located above the local star-forming sequence, biasing the stacked spectrum towards the high-redshift star-forming sequence (Fig. 1). Therefore, this data point (the circle point with 'x' symbol in Fig. 1) is discarded from further analysis. We detect the [O\,\textsc{iii}] $\lambda4363$ emission line at S/N > 10 in four of the stacked spectra of the SDSS reference galaxies and in six of the stacked spectra of the local analogues (the open circles with crosses in Fig. 1. The He\,\textsc{ii} $\lambda4686$ lines are all well detected (S/N > 10) in all the stacking spectra. We refer readers to section 3 in Bian et al. (2018) for more detail for the procedure on stacked spectra, subtracting the stellar continuum, and emission line fitting.

3 RESULTS

3.1 N-to-O ratios

The stacked spectra enable us to study both the N/O ratio and the oxygen abundance in the local analogues and the local reference galaxies using the direct T_e method. The T_e method provides the most reliable ways to measure the N/O ratio and oxygen abundance. However, it is extremely challenging to measure the N/O ratio and oxygen abundance using the T_e method in high-redshift galaxies (e.g. Sanders et al. 2016b; Kojima et al. 2017; Strom et al. 2017), because it requires a detection of the weak emission line [O\,\textsc{iii}] $\lambda4363$, which is more than 10 times weaker than Hβ. However, such measurements are possible in this work, thanks to the high S/N in the stacked spectra of both the local analogues and the SDSS reference galaxies.

We compute the N/O ratio and oxygen abundance using the Izotov et al. (2006) recipe. The electron temperature in the O^{++} zone ($T_3(\text{O})$) is derived using the [O\,\textsc{iii}] $\lambda\lambda4959,5007$/[O\,\textsc{iii}] $\lambda4363$ ratio. For the electron temperature in the O$^+$ zone ($T_2(\text{O})$), the relation between T_3 and T_2 is adopted from Campbell, Terlevich & Melnick (1986) as follows: $T_2 = 0.7T_3 + 3000$ K. Our main conclusion is not sensitive to the T_3–T_2 relation used. We estimate O^{++} and O$^+$ abundance based on the electron temperatures in the corresponding regions. The final oxygen abundance is derived by adding O^{++} and O$^+$ abundance together. For the nitrogen abundance, we assume that the electron temperature in the N$^+$ zone is the same as that in the O$^+$ zone, $t_2(\text{N}) = t_2(\text{O})$ (e.g. Kennicutt, Bresolin & Garnett 2003). We derive the N$^+$/O$^+$ ratio based on the $T_2(\text{N})$ and $T_2(\text{O})$, and the N$^+$/O$^+$ ratio is a good approximation to the N/O ratio (Andrews & Martini 2013).

Fig. 2 shows the relation between N/O ratio and the oxygen abundance in the local analogues (blue data points) and the SDSS reference galaxies (red data points). The relation consists of two regimes: the primary nitrogen regime, where the N/O ratio is a constant at $12 + \log(\text{O/H}) < 8.2$. The secondary nitrogen regime, where the N/O ratio increase with oxygen abundance at $12 + \log(\text{O/H}) > 8.2$ (e.g. van Zee, Salzer & Haynes 1998).

The N/O ratios for the two samples of galaxies in the primary nitrogen regime are estimated by averaging the N/O ratios in the range $12 + \log(\text{O/H}) < 8.2$. We find that, in the primary N regime, the N/O ratios in the local analogues are higher than those in the local reference galaxies by ~0.1 dex at -1.43 ± 0.01 and -1.53 ± 0.01, respectively. The N/O offset between the local analogues and the SDSS reference galaxies in the secondary nitrogen regime is also at the similar level, but it is difficult to quantify the difference based on a few data points in this regime. The N/O offset is similar to that in green pea galaxies (e.g. Amorín, Pérez-Montero & Vílchez
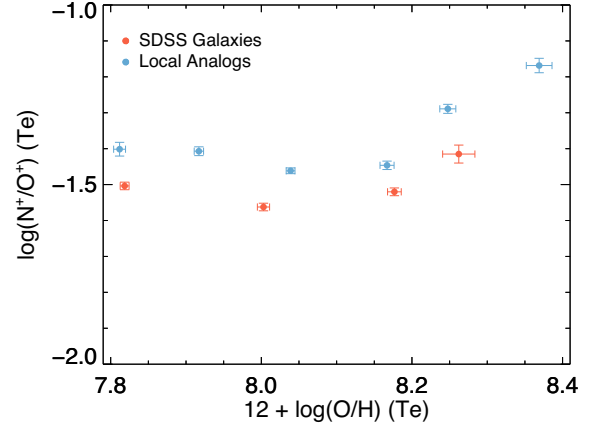

Figure 2. N$^+$-to-O$^+$ ratio as a function of oxygen abundance in the local analogues of high-redshift galaxies (blue data points) and the SDSS reference galaxies (red data points). The N$^+$-to-O$^+$ ratio is an approximation to the N-to-O ratio (e.g. Andrews & Martini 2013). Both N$^+$-to-O$^+$ ratio and oxygen abundance based on the direct T_e method. The data points from left to right correspond to increasing [N\,\textsc{ii}] $\lambda6584$/Hα ratio direction. A colour version of this figure is available online.

2010). Studies suggest that it requires the change of N/O by 0.2–0.4 dex to shift the BPT star-forming locus at $z \sim 0$ to that at $z \sim 2.3$ (e.g. Masters et al. 2016). The N/O enhancement in the high-redshift analogues cannot fully explain the offset between the local analogues and the SDSS galaxies. Strom et al. (2017) also found an ~0.1 dex offset between $z \sim 2$ star-forming galaxies and local galaxies using strong emission lines, and these authors also suggested the offset between $z \sim 2$ and local star-forming galaxies on the BPT diagram cannot fully account for the N/O enhancement.

It is worth noting that our main conclusion will not change, if we adopt different recipes to estimate $T_3(\text{O})$ (e.g. Pagel et al. 1992), different T_3–T_2 relations (e.g. López-Sánchez et al. 2012), and different $t_2(\text{N})$–$t_2(\text{O})$ relations (e.g. Berg et al. 2015).

3.2 Spectral hardness

The spectral hardness can be studied using the He\,\textsc{ii} $\lambda4686$ emission line, because the ionization potential of He^{++} is 54.4 eV, thus the He\,\textsc{ii} $\lambda4686$ emission line is very sensitive to the hard ionizing radiation field. Fig. 3 shows the stacked spectra around He\,\textsc{ii} $\lambda4686$ in the high-redshift analogues and local reference galaxies in six [N\,\textsc{ii}]/Hα bins in the range of $-2.00 < \log([\text{N\,\textsc{ii}}] \lambda6584/\text{H}\alpha) < -0.50$. We fit the He\,\textsc{ii} $\lambda4686$ line with other nearby emission lines, including [Fe\,\textsc{iii}] and [Ar\,\textsc{iv}] simultaneously. We firmly (S/N > 10) detect the He\,\textsc{ii} $\lambda4686$ in all stacked spectra. The He\,\textsc{ii} $\lambda4686$ line width is $\sigma = 100$–200 km s^{-1} without obvious underlying broad component (Fig. 3). The emission line width of He\,\textsc{ii} is consistent with that of Hβ in the N2 bins with N2 < -1.25. However, when N2 > -1.25, the He\,\textsc{ii} line width is systematically larger than Hβ line width by about 50 km s^{-1} in velocity dispersion. The He\,\textsc{ii} line width suggests that the He\,\textsc{ii} $\lambda4686$ emission is mostly raised from nebular emission at N2 < -1.25, and at N2 > -1.25 the atmospheric emission in Wolf–Rayet stars also starts to contribute to the He\,\textsc{ii} $\lambda4686$ emission, however, the He\,\textsc{ii} $\lambda4686$ emission in Wolf–Rayet is not the dominate component of the He\,\textsc{ii} $\lambda4686$ emission in these galaxies due to relatively narrow He\,\textsc{ii} $\lambda4686$ line width, a few hundred km s^{-1} rather than a few thousand km s^{-1}.
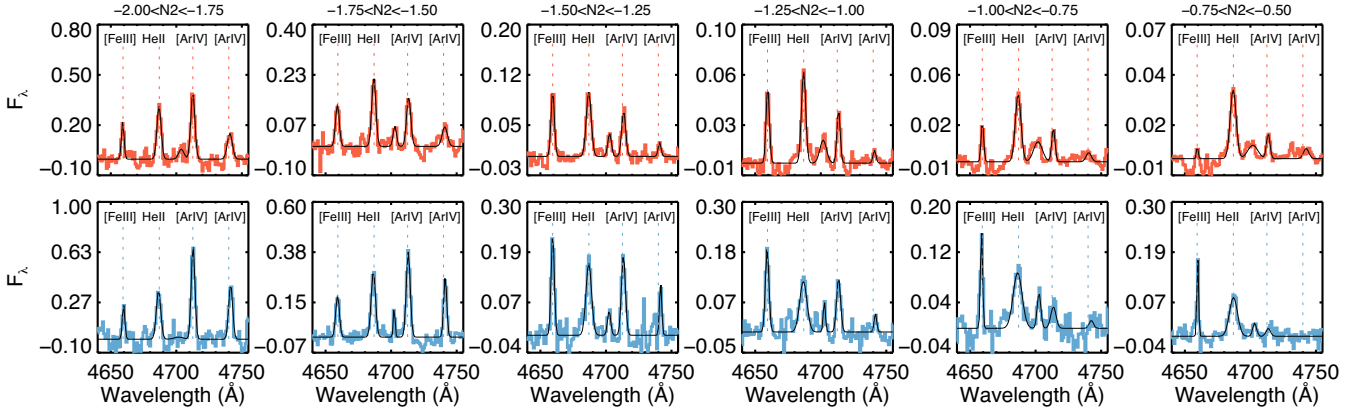
Figure 3. The He II λ4686 spectra of the SDSS reference galaxies (top panel) and the local analogues of high-redshift galaxies (bottom panel) in different [N II] λ6584/Hα bins. The log [N II] λ6584/Hα (N2) increases from left to right. The rightmost panel is for the bin of $-0.75 < \log([\text{N II}]\,\lambda6584/\text{H}\alpha) < -0.50$, and the leftmost panel is for the bin of $-2.00 < \log([\text{N II}]\,\lambda6584/\text{H}\alpha) < -1.75$. A colour version of this figure is available online.
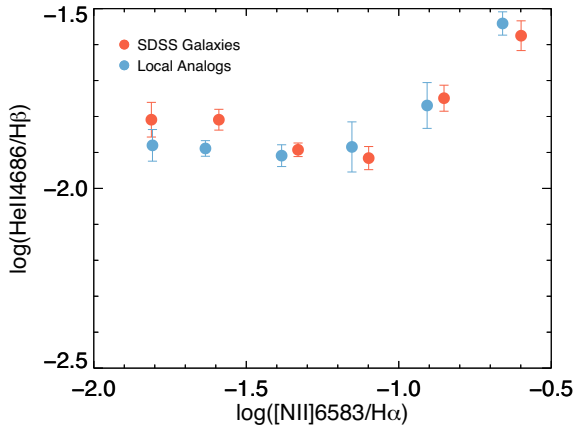
Figure 4. He II λ4686/Hβ versus [N II] λ6584/Hα diagram of the local analogues of high-redshift galaxies (blue data points) and the SDSS reference galaxies (red data points). The black lines are the best-fitting Gaussian models of the emission lines. A colour version of this figure is available online.

Figure 5. Ionization parameter versus $\log([\text{N II}]\,\lambda6584/\text{H}\alpha)$ in the local analogues of high-redshift galaxies (blue data points) and the SDSS reference galaxies (red data points). A colour version of this figure is available online.

Fig. 4 shows the He II λ4686/Hβ ratio as a measure of spectral hardness in the local analogues and the SDSS reference galaxies in different [N II]/Hα bins. For $\log([\text{N II}]/\text{H}\alpha) < -1.2$, the He II λ4686/Hβ slightly decreases with increasing [N II]/Hα ratio, but then slightly increases with further increase in the [N II]/Hα ratio. This increase is presumably correlated with a greater fraction of W–R stars at higher metallicity. This trend is generally consistent with that found in the individual galaxies with He II λ4686 detection (Shirazi & Brinchmann 2012). We notice that the He II λ4686/Hβ ratio in the stacked is slightly (<0.5 per cent) higher than the He II λ4686/Hβ ratio measured in the individual SDSS galaxies (Shirazi & Brinchmann 2012), especially at the high [N II]/Hα end. This could be due to the high S/N spectra of the stack spectra, which allows us better fitting the flux from underlying weak broad component of the He II λ4686 emission line.

We find that the He II λ4686/Hβ values of the local analogues and the SDSS reference galaxies are consistent with each other in all the [N II]/Hα bins, suggesting that the local analogues of high-redshift galaxies and the SDSS reference galaxies share a similar shape of the ionizing radiation field.
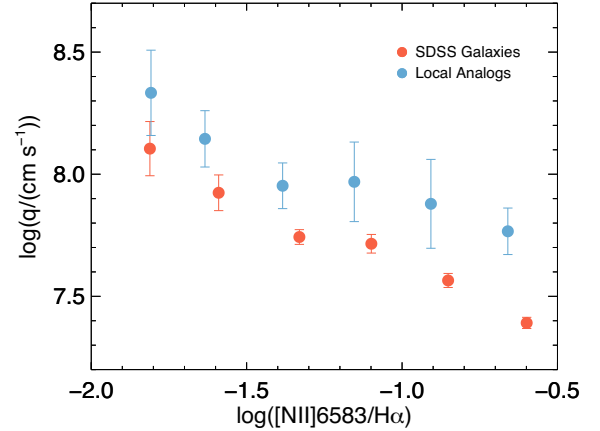
3.3 Ionization parameter

The ionization parameter is estimated for each stacked spectrum using the $O32 = ([\text{O III}]\,\lambda\lambda4959,5007/[\text{O II}]\,\lambda3727)$ and $R23 = [([\text{O II}]\,\lambda3727 + [\text{O III}]\,\lambda\lambda4959,5007)/\text{H}\beta]$ ratios. We adopt the Kobulnicky & Kewley (2004) recipe to compute the metallicity and the ionization parameter iteratively until the metallicity converges. We refer readers to Kobulnicky & Kewley (2004) and Kewley & Ellison (2008) for more details.

Fig. 5 shows the ionization parameter as a function $\log([\text{N II}]/\text{H}\alpha)$ in the local analogues and the local reference galaxies. In both galaxy samples, the ionization parameters decrease with [N II]/Hα. The local analogues have significantly higher ionization parameters than the local reference galaxies in all $\log([\text{N II}]/\text{H}\alpha)$ bins. The mean difference of ionization parameters between the local analogues and local reference galaxies is 0.27 ± 0.05 dex. The difference of the ionization parameter increases with [N II]/Hα. In the highest [N II]/Hα bin, the ionization parameter in the local analogues is 0.38 ± 0.09 dex higher than that in the local reference galaxies, and the difference of ionization parameter becomes 0.23 ± 0.20 dex in the lowest [N II]/Hα bin. The ionization

parameter plays a major role to drive the BPT evolution with redshift, particularly at the high-metallicity end.

By applying photoionization models to cosmological zoom-in simulations, Hirschmann et al. (2017) found a similar result that evolution of the [O III] λ5007/H β versus [N II] λ6584/H α emission ratios is mainly driven by ionization parameters. In their models, the ionization parameter is directly regulated by the SFR. This is in agreement with the observational studies that have shown the ionization parameter increases with SFR and specific SFR (SFR/M_*) (e.g. Kaasinen et al. 2018). Our high-redshift analogues also have high specific SFR (Bian et al. 2016) and follow the $z \sim 2.3$ M_*–SFR relation (Sanders et al. 2020). Thus, the high (specific) SFR is the main physical origin to drive the high ionization parameter and the evolution of the [O III] λ5007/H β versus [N II] λ6584/H α emission ratios.

4 DISCUSSION

4.1 Origin of He II emission

The He II λ4686 emission strength is a few per cent of H β in the stacked spectra in both the high-redshift analogues and local reference galaxies. This strength is similar to that in the individual galaxies that were selected from the SDSS survey based on their strong He II λ4686 emissions (Shirazi & Brinchmann 2012). Such strong He II λ4686 emission is proposed to arise from the atmosphere of Wolf–Rayet stars and/or nebular emission due to the hard radiation field emitted from the Wolf–Rayet stars. However, the lifetime of Wolf–Rayet stars is short, on the order of ∼2 Myr. Given this, Wolf–Rayet galaxies should only be a short transitional phase of galaxies, and only a small fraction of galaxies should contribute to the He II λ4686 emission when stacking the spectra. Therefore, the He II λ4686/H β ratio in the stacked spectra should be significantly smaller than that in the individual Wolf–Rayet galaxies. The similar strength of the He II λ4686 in the stacked spectra and individual Wolf–Rayet galaxies suggests that the He II λ4686 emission commonly exists in a majority of these populations of galaxies and is unlikely due to the hard radiation field of Wolf–Rayet stars. Furthermore, the He II λ4686 emissions in the stacked spectra are narrow with $\sigma = 100$–200 km s^{-1} with no obvious broad component, associated with strong Wolf–Rayet stars (e.g. Miralles-Caballero et al. 2016).

We consider the following potential sources to produce the He II λ4686 emissions.

(i) A hard radiation field from AGNs or shocks can excite the He II λ4686 emission. Shocks and AGNs move galaxies from the star-forming sequence to the AGN/shock region in the BPT diagnostic diagrams. In Section 2.1, we selected galaxies in all three BPT diagrams to minimize the AGN/shock contamination. In particular, the SDSS reference galaxy sample is located right on the local star-forming sequence on the BPT diagram and well separated from the AGN and shock regions. Therefore, shocks and AGNs contribution should be negligible in both the local analogues and the SDSS reference galaxies.

(ii) X-ray binaries can provide a hard radiation field to produce He II λ4686 emission. Kaaret, Ward & Zezas (2004) studied the nebular close to an ultraluminous X-ray source in Holmberg II and establish a relation between the nebular He II λ4686 and X-ray luminosity, $L_{He\,II} \sim 10^{-3} L_{X\text{-ray}}$, using CLOUDY photoionization models. X-ray luminosity in star-forming galaxies is dominated by X-ray emission from the high-mass X-ray binaries. In this situation,

X-ray luminosity can be used as a star formation rate indicator (e.g. Ranalli, Comastri & Setti 2003). We connect the X-ray luminosity to H β luminosity, $L_{X\text{-ray}} \sim 10^{-2} L_{H\beta}$, which leads to $L_{He\,II} = 10^{-6} L_{H\beta}$. Therefore, we estimate the He II λ4686 emission from the X-ray binaries to be four orders of magnitude smaller than that in the stacked spectra.

(iii) The hard radiation field is due to binary stars and/or fast-rotating stars. Integrating the binary stars and stellar rotation in the stellar synthesis models could significantly change the stellar evolution track of massive stars and increase their lifetime (e.g. Eldridge & Stanway 2009). Therefore, binary evolution models result in the presence of massive stars (e.g. Wolf–Rayet stars) for a wider range of ages, which likely increases the contribution from stellar He II λ4686 emission in the stacked spectra. In the stellar synthesis models taking binary evolution into account (e.g. BPASS), the time-scale over which stars can produce He^{++} ionizing photons is on the order of 100 Myr, which is two orders of magnitude higher than that derived from the stellar synthesis models that do not take binary evolution into account (e.g. Wofford et al. 2016). The flux ratio of He II λ4686 to H β has been measured in individual H II regions using deep optical spectra to be on the order of one per cent level (e.g. Berg et al. 2015). Given this, we believe the He II λ4686 emission is mostly likely due to the hard radiation field from massive stars, particularly when taking the binary evolution models into account. Such a scenario has also been used to explain the nebular emission lines requiring similar high excitation energies, such as He II1640, C IV1549, C III]1909, detected in both low- and high-redshift galaxies (e.g. Stark et al. 2014, 2015; Senchyna et al. 2017).

5 CONCLUSION

We study the physical origins of the offset between the low- and high-redshift galaxies on the [O III] λ5007/H β versus [N II] λ6584/H α BPT diagram. We select a sample of local analogues of high-redshift galaxies and the local reference galaxies from the SDSS survey based on their location of the BPT diagram. The SDSS reference galaxy located on the local star-forming BPT sequence, and the local analogue galaxies located on the high-redshift star-forming BPT sequence. The local analogues well resemble the physical properties of high-redshift star-forming galaxies, provide an ideal laboratory to study what causes the evolution of star-forming BPT sequence from high to low redshift.

Using the [O III] λ4363 and He II λ4686 weak emission lines in the stacked spectra, we found (1) the N/O ratios in the local analogues of high-redshift galaxies are ∼0.1 dex higher than those in the SDSS reference galaxies, which play a minor role (25 per cent–50 per cent) to drive the offset on the BPT diagram; (2) the ionization parameters in the local analogues are 0.3–0.4 dex higher than those in the SDSS reference galaxies, which are the major cause (50 per cent–75 per cent) of the offset on the BPT diagram; (3) the local analogues and the SDSS reference have similar hard ionizing radiation field. This hard radiation is mostly likely to originate from stars with significant rotation and/or in binary systems.

REFERENCES

Amorín R. O., Pérez-Montero E., Vílchez J. M., 2010, ApJ, 715, L128

Andrews B. H., Martini P., 2013, ApJ, 765, 140

Baldwin J. A., Phillips M. M., Terlevich R., 1981, PASP, 93, 5

Berg D. A., Skillman E. D., Croxall K. V., Pogge R. W., Moustakas J., Johnson-Groh M., 2015, ApJ, 806, 16

Bian F. et al., 2010, ApJ, 725, 1877

Bian F., Kewley L. J., Dopita M. A., Juneau S., 2016, ApJ, 822, 62

Bian F., Kewley L. J., Dopita M. A., 2018, ApJ, 859, 175

Brinchmann J., Pettini M., Charlot S., 2008, MNRAS, 385, 769

Campbell A., Terlevich R., Melnick J., 1986, MNRAS, 223, 811

Cid Fernandes R., Mateus A., Sodré L., Stasińska G., Gomes J. M., 2005, MNRAS, 358, 363

Dopita M. A., Kewley L. J., Sutherland R. S., Nicholls D. C., 2016, Ap&SS, 361, 61

Eldridge J. J., Stanway E. R., 2009, MNRAS, 400, 1019

Erb D. K., Shapley A. E., Pettini M., Steidel C. C., Reddy N. A., Adelberger K. L., 2006, ApJ, 644, 813

Hainline K. N., Shapley A. E., Kornei K. A., Pettini M., Buckley-Geer E., Allam S. S., Tucker D. L., 2009, ApJ, 701, 52

Hirschmann M., Charlot S., Feltre A., Naab T., Choi E., Ostriker J. P., Somerville R. S., 2017, MNRAS, 472, 2468

Izotov Y. I., Stasińska G., Meynet G., Guseva N. G., Thuan T. X., 2006, A&A, 448, 955

Jones T., Martin C., Cooper M. C., 2015, ApJ, 813, 126

Juneau S. et al., 2014, ApJ, 788, 88

Kaaret P., Ward M. J., Zezas A., 2004, MNRAS, 351, L83

Kaasinen M., Kewley L., Bian F., Groves B., Kashino D., Silverman J., Kartaltepe J., 2018, MNRAS, 477, 5568

Kauffmann G. et al., 2003, MNRAS, 346, 1055

Kennicutt R. C., Jr., Bresolin F., Garnett D. R., 2003, ApJ, 591, 801

Kewley L. J., Ellison S. L., 2008, ApJ, 681, 1183

Kewley L. J., Dopita M. A., Sutherland R. S., Heisler C. A., Trevena J., 2001, ApJ, 556, 121

Kewley L. J., Groves B., Kauffmann G., Heckman T., 2006, MNRAS, 372, 961

Kewley L. J., Dopita M. A., Leitherer C., Davé R., Yuan T., Allen M., Groves B., Sutherland R., 2013a, ApJ, 774, 100

Kewley L. J., Maier C., Yabe K., Ohta K., Akiyama M., Dopita M. A., Yuan T., 2013b, ApJ, 774, L10

Kobulnicky H. A., Kewley L. J., 2004, ApJ, 617, 240

Kojima T., Ouchi M., Nakajima K., Shibuya T., Harikane Y., Ono Y., 2017, PASJ, 69, 44

Liu X., Shapley A. E., Coil A. L., Brinchmann J., Ma C.-P., 2008, ApJ, 678, 758

López-Sánchez Á. R., Dopita M. A., Kewley L. J., Zahid H. J., Nicholls D. C., Scharwächter J., 2012, MNRAS, 426, 2630

Masters D. et al., 2014, ApJ, 785, 153

Masters D., Faisst A., Capak P., 2016, ApJ, 828, 18

Miralles-Caballero D. et al., 2016, A&A, 592, A105

Nakajima K., Ouchi M., 2014, MNRAS, 442, 900

Pagel B. E. J., Simonson E. A., Terlevich R. J., Edmunds M. G., 1992, MNRAS, 255, 325

Ranalli P., Comastri A., Setti G., 2003, A&A, 399, 39

Rodighiero G. et al., 2011, ApJ, 739, L40

Salim S., Lee J. C., Davé R., Dickinson M., 2015, ApJ, 808, 25

Sanders R. L. et al., 2016a, ApJ, 816, 23

Sanders R. L. et al., 2016b, ApJ, 825, L23

Sanders R. L. et al., 2020, MNRAS, 491, 1427

Senchyna P. et al., 2017, MNRAS, 472, 2608

Shapley A. E. et al., 2015, ApJ, 801, 88

Shirazi M., Brinchmann J., 2012, MNRAS, 421, 1043

Stark D. P. et al., 2014, MNRAS, 445, 3200

Stark D. P. et al., 2015, MNRAS, 450, 1846

Stasińska G., Cid Fernandes R., Mateus A., Sodré L., Asari N. V., 2006, MNRAS, 371, 972

Steidel C. C. et al., 2014, ApJ, 795, 165

Steidel C. C., Strom A. L., Pettini M., Rudie G. C., Reddy N. A., Trainor R. F., 2016, ApJ, 826, 159

Strom A. L., Steidel C. C., Rudie G. C., Trainor R. F., Pettini M., Reddy N. A., 2017, ApJ, 836, 164

Trainor R. F., Strom A. L., Steidel C. C., Rudie G. C., 2016, ApJ, 832, 171

van Zee L., Salzer J. J., Haynes M. P., 1998, ApJ, 497, L1

Veilleux S., Osterbrock D. E., 1987, ApJS, 63, 295

Wofford A. et al., 2016, MNRAS, 457, 4296

This paper has been typeset from a TEX/LATEX file prepared by the author.